Available online at www.sciencedirect.com
SCIENCE DIRECT®
ELSEVIER
International Journal of Multiphase Flow 30 (2004) 803–825
International Journal of Multiphase Flow
www.elsevier.com/locate/ijmulflow

A stochastic description of wall sources in a turbulent field: part 2. Calculation for a simplified model of horizontal annular flows ☆

Yoichi Mito, Thomas J. Hanratty *

Department of Chemical and Biomolecular Engineering, University of Illinois at Urban-Champaign, 205 Roger Adams Laboratory, Box C-3, 600 South Mathews Avenue, Urbana, IL 61801, USA

Received 14 July 2003; received in revised form 22 February 2004

Abstract

A stochastic approach that uses a modified Langevin equation to calculate fluid velocities seen by particles dispersing in a turbulent flow was verified at $Re_\tau = 150$, $V_T^+ = 0.11$, $\tau_p^+ = 20$ in Part 1 of this paper. It is now used to examine the effects of particle inertia and gravitational settling on the deposition rate at $Re_\tau = 590$. The system considered is an idealized annular flow in a horizontal channel. Drops are admitted from the top and the bottom walls at relative rates such that a fully-developed field is realized. The walls are considered to be arrays of point sources. The theoretical problem is to model the behavior of an instantaneous wall source. Particles are ejected from the source with a velocity V_i^0 at time zero. They are mixed by the fluid turbulence and eventually deposit at the top and bottom walls. Of particular interest are the strong effect of very small gravitational settling on the rate of deposition and the definition of a critical condition for particles (ejected from the bottom wall) to reach the top wall to create an annular flow.

Keywords: Horizontal annular flow; Wall source; Fully-developed concentration field; Langevin equation; Rate of deposition; Gravitational settling; Free-flight; Turbulent impaction

☆ We are pleased to have this paper included in the George Yadigaroglu Festschrift Volume since this is a way to thank him for his many contributions to the area of multiphase flow. His impeccable efforts as an Associate Editor of the International Journal of Multiphase Flow are noteworthy.

* Corresponding author. Tel.: +1-217-333-1318; fax: +1-217-333-5052.
E-mail address: hanratty@scs.uiuc.edu (T.J. Hanratty).

0301-9322/$ - see front matter © 2004 Elsevier Ltd. All rights reserved.
doi:10.1016/j.ijmultiphaseflow.2004.02.003

1. Introduction

A critical issue in describing the behavior of gas–liquid annular flow in a horizontal conduit is the understanding of the effect of gravity on the mixing of drops in the gas core and on the rate of deposition of drops on the films flowing along the walls. Improved theories for these processes will help in calculating the entrainment of liquid in the gas core and the asymmetric distribution of the liquid film flowing along the wall. Of particular practical importance is the understanding of temperature variation around the circumference in heat transfer systems.

The expectation is that gravity would enhance deposition velocities at the bottom of the pipe and decrease deposition velocities at the top. Gravity can also cause drops to have larger concentrations. This can greatly increase the rates of deposition at the bottom of the pipe and decrease the entrainment from what would be observed in a vertical pipe (Pan and Hanratty, 2002). When the effects of gravitational settling are very much greater than the mixing due to gas phase turbulence, drops are unable to reach the top of the pipe. A consideration of this phenomenon was used by Baik and Hanratty (2003) to define the transition from stratified to annular flow in large diameter pipes.

Despite the central importance of dispersion and deposition in horizontal flows, experimental studies which define the mechanisms are sparse. This paper presents results of numerical experiments which define the influence of gravity on the deposition constant. In a subsequent paper droplet concentration profiles will be discussed. In order to define mechanisms more clearly, the simplified system shown in Fig. 1 is considered. It is an infinitely wide rectangular channel for which the half-height is H. The flow is fully-developed. The drops are represented by solid spheres that are injected with a velocity V_1^0, V_2^0, V_3^0 from the bottom wall at a rate per unit area of R_{Ab} and with a velocity V_1^0, $-V_2^0$, V_3^0 from the top wall, where the flux is designated as R_{At}. The particles are removed from the field when they are a distance of $d_{\mathrm{p}}/2$ from a wall, where d_{p} is their diameter. Under a fully-developed condition

$$R_{\mathrm{Ab}} = R_{\mathrm{Db}} \quad \text{and} \quad R_{\mathrm{At}} = R_{\mathrm{Dt}}, \tag{1}$$

where R_{Db} and R_{Dt} are the deposition fluxes at the bottom and top walls. The system defined above has the property that the net fluxes at both walls and at all locations in the channel are zero. This greatly simplifies the representation of the concentration field in terms of fundamental mechanisms responsible for particle mixing.

A Lagrangian approach is used to carry out the calculations. The top and bottom walls are represented by summing the contributions of arrays of sources which entered the field at dif-

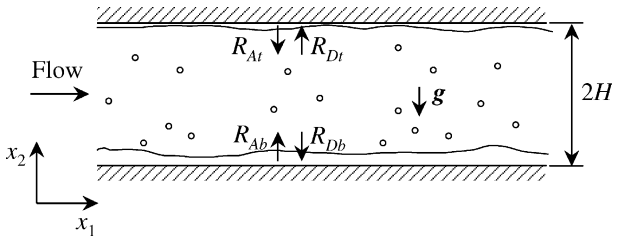

Fig. 1. Gas–liquid annular flow in a horizontal channel.

ferent times, $t \geqslant 0$. As time becomes large, a fully-developed condition is reached for which the sum is not changing with time. The theoretical problem, then, is to describe the behavior of instantaneous point sources at the bottom and top walls. The critical issue is the representation of the fluid turbulence seen by a dispersing particle. This is done by using a modified Langevinequation, as had been explored previously by Perkins (1992), Sommerfeld et al. (1993), Pozorski and Minier (1998) and Iliopoulos et al. (2003) for instantaneous sources located in the fluid. The last of these references carried out experiments in a DNS of turbulent flow in a channel and paid particular attention to the spatial variation of the fluid turbulence close to a wall.

In a recent paper on "A stochastic description of wall sources in a turbulent field: part 1 Verification" (Mito and Hanratty, 2003), the approach was tested by comparing calculations at a Reynolds number of $Re_\tau = Hv^*/v = 150$ and a dimensionless terminal velocity of $V_T^+ = V_T/v^* = 0.11$ (where v^* is the friction velocity and v is the kinematic viscosity of the continuous phase) in which the fluid turbulence is given by a DNS and by a modified Langevin equation. The results of this comparison prompted the present study which was carried out at a higher Reynolds number, $Re_\tau = 590$, and over wider ranges of terminal velocities, inertial time constants. The scaling laws defining the Lagrangian time constants were explored in Part 1 of this paper and in a paper by Mito and Hanratty (2002).

The few early studies of horizontal annular flows are summarized by McCoy and Hanratty (1977). Since then, one can only cite the measurements of droplet concentration profiles in gas–liquid annular flows by Williams et al. (1996) and by Paras and Karaberas (1991). The calculations presented for $V_T = 0$ are analogous to the computer studies in a DNS or a LES in a vertical flow by Brooke et al. (1994), Chen and McLaughlin (1995), Wang et al. (1997) and Narayanan et al. (2003). These considered the subsequent behavior of uniformly distributed sources at time zero in a channel flow. The first three involved a transient process for which the number of particles in the field decreases with time. Narayanan et al. (2003) considered a fully-developed field by continuing to provide sources in the bulk flow. To our knowledge the numerical study described in this paper is the only one for which wall sources are considered. Zhang and Ahmadi (2000) carried out experiments in a DNS, which included the influence of gravitational settling, by seeding particles into the flow at time zero. This study is of interest in that it shows that gravity can increase the deposition constant. Mechanisms are not discussed and the range of variables is not as large as considered in this study.

2. Calculation of particle trajectories

Since particles that are much heavier than the fluid are being considered their velocity and location are defined with the following equations:

$$\frac{dx_i}{dt} = V_i, \tag{2}$$

$$\frac{dV_i}{dt} = -\frac{3\rho_f C_D}{4 d_p \rho_p} |\boldsymbol{V} - \boldsymbol{U}|(V_i - U_i) + g_i, \tag{3}$$

where x_i is the displacement of the particle, V_i is the velocity of the particle, U_i is the gas velocity seen by the particle, t is the time, ρ_p is the density of the particle, ρ_f is the density of the gas, and g_i is a component of the acceleration of gravity. In the system shown in Fig. 1, x_1, x_2 and x_3 are assigned to the coordinates in the streamwise, wall-normal and spanwise directions, respectively. Then $g_2 = -g$ and $g_1 = g_3 = 0$, where g is the magnitude of the acceleration of gravity. The drag coefficient, C_D, is given by

$$C_D = \frac{24}{Re_p}\left(1 + 0.15Re_p^{0.687}\right), \tag{4}$$

where the particle Reynolds number, Re_p, is defined with d_p and the magnitude of the relative velocity $|\boldsymbol{U} - \boldsymbol{V}|$. With the assumption that the concentrations of particles are small, inter-particle collisions and the influence of the particles on the fluid turbulence are ignored.

3. Stochastic simulation at $Re_\tau = 590$

A modified Langevin equation is used to calculate the change of the fluid velocity fluctuation seen by a solid particle, du_i, over a time interval dt:

$$d\left(\frac{u_i}{\sigma_i}\right) = -\frac{u_i}{\sigma_i \tau_i}\mathrm{d}t + \overline{d\mu_i} + d\mu_i', \tag{5}$$

where u_i is the fluctuating component of the fluid velocity seen by the particle, σ_i is the Eulerian root-mean-square value of the velocity fluctuation, τ_i is the Lagrangian time constant. The forcing function, $d\mu_i$, is assumed to be jointly Gaussian (Mito and Hanratty, 2002). The mean drift, $\overline{d\mu_i}$, and the covariances of the fluctuations are given as

$$\overline{d\mu_i} = \frac{\partial\left(\frac{\overline{u_2 u_i}}{\sigma_i}\right)}{\partial x_2}\mathrm{d}t, \tag{6}$$

$$\overline{d\mu_i' d\mu_j'} = \frac{\overline{u_i u_j}}{\sigma_i \sigma_j}\left(\frac{1}{\tau_i} + \frac{1}{\tau_j}\right)\mathrm{d}t, \tag{7}$$

where an overbar indicates an ensemble average. (It is noted that the nonzero terms in Eqs. (6) and (7) are $\overline{d\mu_1}$, $\overline{d\mu_2}$, $\overline{d\mu_1'^2}$, $\overline{d\mu_2'^2}$, $\overline{d\mu_3'^2}$, $\overline{d\mu_1' d\mu_2'}$ for the flow field that is considered.) These equations and the numerical procedure for solving them are described, in detail, in Part 1. The DNS database for turbulent channel flow at $Re_\tau = 590$, obtained by Moser et al. (1999), is used to provide the mean velocities of the fluid and the turbulent statistics that appear in Eqs. (5)–(7). The computational time step used in Eqs. (2), (3), (5) was $\Delta t^+ = \Delta t v^{*2}/\nu = 0.5$.

We follow the simple approach, described in Part 1, that uses time constants characterizing the dispersion of fluid particles to define τ_i. Since the Lagrangian time constants that are determined from a DNS are not available at $Re_\tau = 590$, a scaling law (Monin and Yaglom, 1975; Tennekes, 1979) is used to specify them in the outer region, $x_2^+ \ (= x_2 v^*/\nu) \geqslant 100$:

$$\tau_i = \frac{2\sigma_i^2}{C_0 \tilde{\varepsilon}}. \tag{8}$$

Here $\tilde{\varepsilon}$ is a modified dissipation rate of turbulent energy defined as

$$\tilde{\varepsilon} = \nu \left\{ \overline{\frac{\partial u_i}{\partial x_j}} \overline{\frac{\partial u_i}{\partial x_j}} - 2 \left(\frac{\partial \sqrt{k}}{\partial x_j} \right)^2 \right\}, \tag{9}$$

where k is the turbulent energy. In the near-wall region, $x_2^+ \leqslant 40$, the time constants determined in a DNS at $Re_\tau = 300$ (Mito and Hanratty, 2002) are used. A linear interpolation between these inner and outer laws is used to represent τ_i in the region $40 < x_2^+ < 100$.

Fig. 2a shows τ_2^+ values calculated from a DNS at $Re_\tau = 150$ and 300 (Mito and Hanratty, 2002). It is noted that, when plotted against x_2^+, there is a rough agreement out to $x_2^+ = 40$. Calculations based on Eq. (8), with $C_0 = 3.5$, are also shown in Fig. 2b. It is noted that this scaling law provides a rough estimate of $\tau_2 v^*/H$ for $x_2/H \geqslant 0.3$ ($x_2^+ \geqslant 100$) at $Re_\tau = 300$. Values of τ_1^+, τ_2^+, τ_3^+ used in this investigation for $Re_\tau = 590$ are shown in Fig. 3. These were obtained by using the calculations for τ_i^+ for $x_2^+ \leqslant 40$, Eq. (8) with $C_0 = 3.5$ for $x_2^+ \geqslant 100$ and a linear interpolation.

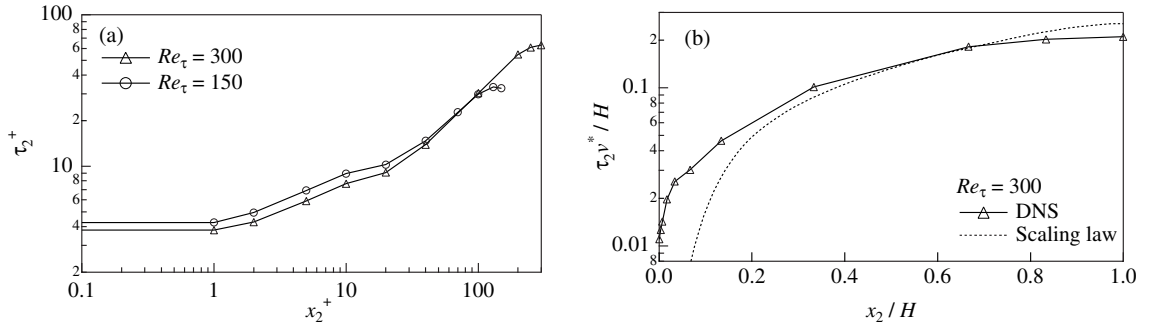

Fig. 2. (a) Lagrangian time constants for the wall-normal fluid velocity fluctuations, seen by the solid particles, that were determined in DNS experiments and (b) a comparison of $Re_\tau = 300$ results with Eq. (8) using $C_0 = 3.5$.

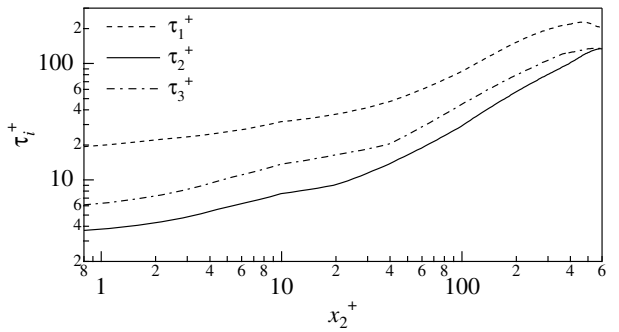

Fig. 3. Lagrangian time constants for the fluid velocity fluctuations, seen by the solid particles, that were used in the Langevin equation at $Re_\tau = 590$.

4. Theoretical considerations

4.1. Parameterization

The primary goal of this study is to determine the effect of gravity on the spatial distribution of particles and on the mechanisms defining rates of deposition for the horizontal system defined in Fig. 1. Since the field is fully-developed the mean concentration, $\overline{C}$, varies only in the x_2 direction. The rate of entrainment from the bottom wall, R_{Ab}, is considered to be fixed so that levels of concentration are expected to decrease with increasing deposition velocities. A dimensionless concentration, defined as $\overline{C}v^*/R_{Ab}$, is calculated as a function of the dimensionless distance from the wall x_2^+.

A bulk concentration can be calculated from these concentration profiles as

$$C_B = \frac{1}{2H}\int_0^{2H} \overline{C}(x_2)\,dx_2. \tag{10}$$

Since

$$2AR_D = AR_{Db} + AR_{Dt}, \tag{11}$$

the total rate of deposition per unit area can be written as

$$R_D = \frac{R_{Ab}}{2}\left(1 + \frac{R_{At}}{R_{Ab}}\right). \tag{12}$$

For the case of $g_2 = 0$ the concentration profile is symmetric, so the rates of atomization at the top and bottom walls are equal and

$$R_D = R_{Ab}. \tag{13}$$

For $g_2 \neq 0$, R_{At}/R_{Ab} is less than unity because of the asymmetric distribution of particles.

A dimensionless deposition constant based on C_B can be defined as

$$\frac{k_{DB}}{v^*} = \frac{R_D}{C_B v^*} = \left[\left(\frac{C_B v^*}{R_{Db}}\right)\left(\frac{R_{Db}}{R_D}\right)\right]^{-1}. \tag{14}$$

The dimensionless groups chosen to define the dependency of k_{DB}/v^* on system variables are $g^+ = gv/v^{*3}$ (or $V_T^+ = V_T/v^*$), $Re_\tau = Hv^*/v$, the dimensionless inertial time constant of the particles $\tau_p^+ = \tau_p v^{*2}/v$, $d_p^+ = d_p v^*/v$, $V_2^{0+} = V_2^0/v^*$. The main calculations were done for a dimensionless particle diameter of $d_p^+ = 0.368$, and for a Reynolds number of $Re_\tau = 590$. Complementary calculations were done for $d_p^+ = 0.736$ and for $Re_\tau = 150$ to examine the effects of d_p^+ and Re_τ. The inertial time constant is defined as

$$\tau_p^+ = \frac{4d_p^+(\rho_p/\rho_f)}{3C_D|\boldsymbol{V}^+ - \boldsymbol{U}^+|}. \tag{15}$$

For Stokes law resistance

$$\tau_p^+ = \frac{d_p^{+2}(\rho_p/\rho_f)}{18}. \tag{16}$$

Thus, if d_p^+ is constant, variations in τ_p^+ correspond roughly to variations of ρ_p/ρ_f. Another choice for representing the inertial time constant would be the bulk average of local values calculated from Eq. (15). For the conditions considered in this paper, Stokes law is approximately valid, so the values calculated from Eq. (16) are used to define τ_p^+. The influence of gravity is represented either by g^+ or by V_T^+, which is the dimensionless free-fall velocity calculated from Eq. (3) on the conditions of $dV_2/dt = 0$ and $\boldsymbol{U} = 0$. An approximation for V_T^+, which is exact for Stokes law resistance, is given as

$$V_T^+ \cong \tau_p^+ g^+. \tag{17}$$

Five particle inertial time constants, $\tau_p^+ = 3$, 5, 10, 20, 40, are considered. At atmospheric conditions these correspond to density ratios, ρ_p/ρ_f, of 400, 665, 1325, 2650 and 5300 for $\tau_p^+ = 3$, 5, 10, 20 and 40. For $d_p^+ = 0.736$ the density ratios are 1/4 of the values given above. The Froude number, Fr $(= v^{*2}/2gH)$, was varied so as to consider free-fall velocities in the range of $0 \leqslant V_T^+ \leqslant 3.2$. For example, the Froude numbers were varied from infinity to 6.9×10^{-4} for $\tau_p^+ = 3$ and from infinity to 9.2×10^{-3} for $\tau_p^+ = 40$. The magnitude of the acceleration of gravity is given as $g^+ = 1/2FrRe_\tau$. Most of the calculations were done for $V_1^{0+} = 15$, $V_2^{0+} = 1$ and $V_3^{0+} = 0$. However, injection velocities with $V_1^{0+} = 0$, 7.5 and with $V_2^{0+} = 0.5$, 2 and 4 were also explored at $Re_\tau = 590$.

4.2. Mechanism of deposition when gravitational effects are not important

4.2.1. Scope

Three mechanisms for deposition can be identified when gravitational effects are not important. One of these is associated with Brownian motion. A second is due to turbulent impaction by particles entrained in the turbulence. A third is the free-flight mechanism whereby particles disengage from the turbulence and move to the wall.

4.2.2. Deposition by Brownian motion

A diffusion coefficient for Brownian motion can by calculated as

$$D = \frac{kT}{3\pi\mu d_p}. \tag{18}$$

where k is the Boltzmann constant, T is the absolute temperature and μ is the viscosity of the continuous phase. From the experiments of Shaw and Hanratty (1977)

$$\frac{k_D}{v^*} = 0.0889Sc^{-0.704}. \tag{19}$$

where Sc is a Schmidt number that is defined as $Sc = \mu/\rho_f D$. From Eqs. (17) and (18), k_D/v^* is calculated for air at atmospheric conditions to vary from 7.6×10^{-6} to 2.8×10^{-7} for d_p varying between 1 μm and 100 μm. These rate constants are 2 to 3 orders of magnitude smaller than the deposition constants characterizing the conditions considered in this paper. Therefore, the effects of Brownian motion were not included in the calculations of the dispersion of particles. McCoy and Hanratty (1977) estimate that this mechanism starts becoming dominant for $\tau_p^+ < 0.2$.

4.2.3. Deposition by turbulent impaction

As shown by Brooke et al. (1994) particles can become trapped in a region very close to the wall where they will have a low level of turbulence induced by the fluid velocity fluctuations. These fluctuations can carry the particles to the wall. Brooke et al. called this a "turbulent diffusion" mechanism.

The length scale representing these turbulent motions is quite small. Therefore, as pointed out by Brooke et al. (1994), one could picture the fluctuations as being influenced by fluid turbulence at a location of about one particle radius from the wall. Thus, the fluid velocity fluctuations seen by these particles should increase with increasing particle diameter. However, the response of the particles to the fluid turbulence should decrease with increasing τ_p^+, which increases with d_p^+. Therefore, the influence of d_p^+ on the average velocity of turbulent impaction is not obvious.

A number of viscous and wall effects which become important when the particles approach the wall (Chen and McLaughlin, 1995) are not taken into account. Consequently, there are some uncertainties about the accuracy of the calculations of turbulent impaction.

4.2.4. Deposition by free-flight

Brooke et al. (1994) and others (Narayanan et al., 2003) have found that particles disengage from the turbulence at different distances from the wall and are launched toward the wall from locations outside the viscous sublayer. These free-flight particles are recognized as having velocities that are much larger than the local fluid velocity fluctuations. They can make large contributions to the flux toward the wall, even though they may constitute a small fraction of the particles. These particles are carried directly to the wall, or they stop short of the wall where they become trapped in a region of low fluid turbulence. For most of the conditions considered in this paper, free-flight particles determine the rate of deposition when the influence of gravity is small. Therefore, it is useful to review the picture of this process that has been presented by Brooke et al. (1994).

Free-flights to the wall can be initiated at different distances from the wall. Fig. 4 depicts a probability density function of the wall-normal velocities of particles which are entrapped in the fluid turbulence at a given x_2. The distribution ignores the presence of particles with large negative

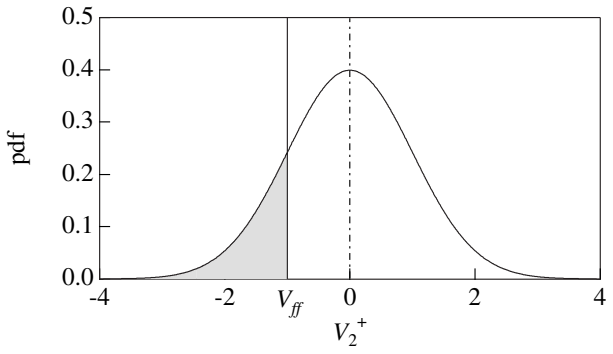

Fig. 4. Velocity distribution of particles at a distance from a wall. The fraction of the particles that start free-flight is represented by the shaded area.

v_2, which started free-flights at larger x_2. An idealized picture of free-flight is that fluid turbulence is having a small effect on the motion toward the wall. Therefore, particles at x_2 have the possibility of starting a free-flight if they have a velocity greater than

$$V_{\mathrm{ff}} = K\frac{x_2}{\tau_{\mathrm{p}}}, \tag{20}$$

where K is of the order of unity ($K = 1$ in a quiescent ambience). These velocities are indicated by the shaded area in Fig. 4. The fraction of the particles, x_{ff}, starting a free-flight would be the fraction of the area under the pdf with velocities greater than V_{ff}. The mean velocity of these particles, $\overline{V}_{\mathrm{ff}}$, is calculated from the first moment. A flux can be defined as $x_{\mathrm{ff}}\overline{V}_{\mathrm{ff}}$ for a unit concentration.

The fraction, x_{ff}, will tend to decrease with increasing x_2 because the particles have a longer distance to travel in order to reach the wall and to increase, because the velocities increase. Since the average velocity, $\overline{V}_{\mathrm{ff}}$, increases with increasing x_2, both x_{ff} and the flux, $x_{\mathrm{ff}}\overline{V}_{\mathrm{ff}}$, can define optimum locations for the initiation of free-flight. Fig. 5 presents plots of $x_{\mathrm{ff}}\overline{V}^{+}_{\mathrm{ff}}$ $(= x_{\mathrm{ff}}\overline{V}_{\mathrm{ff}}/v^*)$ as a function of x_2^+ for different τ_{p}^+, where $K = 1$ is assumed to specify the cutoff velocity defined by Eq. (20). The optimum x_2^+ is seen to increase with τ_{p}^+. For $\tau_{\mathrm{p}}^+ = 40$ it is close to the outer edge of the viscous wall layer and for $\tau_{\mathrm{p}}^+ = 3$ it is at the outer edge of the viscous sublayer. An interesting aspect of Fig. 5 is the large decrease of $x_{\mathrm{ff}}\overline{V}^{+}_{\mathrm{ff}}$ with decreasing τ_{p}^+. The results presented in this figure are consistent with observed large increases in k_{D} with increases in the inertial time constant for $0.2 < \tau_{\mathrm{p}}^+ < 20$ (McCoy and Hanratty, 1977). Calculated values of x_{ff} are given in Fig. 6. These show that only a small fraction of the particles are starting free-flights when τ_{p} is small.

The $\overline{v_2^2}$ (where v_2 is the wall-normal fluctuating component of the particle velocity) used to construct the curves in Figs. 5 and 6 were approximated by using mean-squares of the velocity fluctuations of the fluid $\overline{u_2^2}(x_2)$, calculated from a DNS at $Re_\tau = 150$, and the ratios $\overline{v_2^2}/\overline{u_2^2}$ measured by Lee et al. (1989a,b). The results provide only a qualitative picture of the free-flight process. Inaccuracies arise because of the approximate way of defining the probability distribution of the particle velocities and because of the neglect of the influence of fluid turbulence in calculating drag.

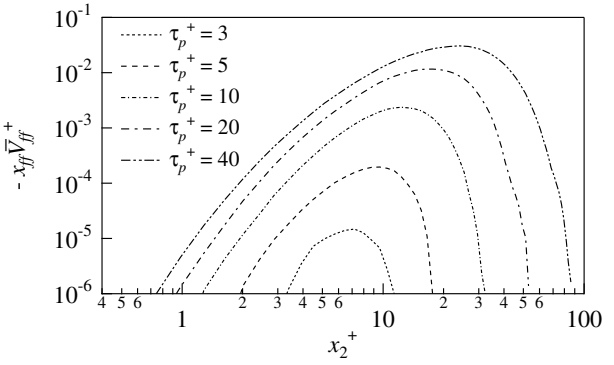

Fig. 5. Contributions of the particles that start free-flight at x_2 to the deposition fluxes.

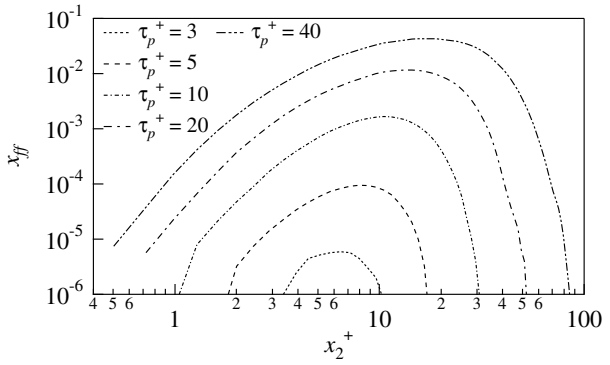

Fig. 6. Fractions of the particles that start free-flight at x_2.

Fig. 5 and laboratory measurements (McCoy and Hanratty, 1977) suggest that k_D/v^* becomes relatively insensitive to changes in τ_p^+ at large τ_p^+. Under these conditions free-flight depositions could be initiated outside the viscous wall layer (say $x_2^+ > 40$) where $\overline{v_2^2}$ is not so strongly dependent on x_2^+ as it is in the viscous wall layer. Therefore, the approximation has been made in previous studies (Hay et al., 1996; Pan and Hanratty, 2002) that k_D can be calculated as the average negative velocity of particles at $x_2^+ \cong 40$. On the assumption that the distribution of the wall-normal velocities of particles is Gaussian and that the mean equals V_T, this approximation gives estimates of k_{DB} and of the mean velocity with which the free-flight particles hit the wall (Pan and Hanratty, 2002):

$$k_{DB} = \frac{\sigma_p}{\sqrt{2\pi}} \exp\left(-\frac{V_T^2}{2\sigma_p^2}\right) + \frac{V_T}{2}\operatorname{erfc}\left(-\frac{V_T}{\sqrt{2}\sigma_p}\right), \tag{21}$$

$$\overline{V}_d = \frac{\sqrt{\frac{2}{\pi}}\sigma_p}{\operatorname{erfc}\left(-\frac{V_T}{\sqrt{2}\sigma_p}\right)} \exp\left(-\frac{V_T^2}{2\sigma_p^2}\right) + V_T, \tag{22}$$

where σ_p is the root-mean-square of the wall-normal velocity fluctuations of the particles.

4.3. Influence of gravitational settling on deposition

4.3.1. Small g_2^+ (or small V_T^+)

Gravitational settling can have an enormous effect on deposition, even at very small V_T^+. The reason for this is that it provides a direct mechanism for the deposition of particles that, otherwise, would be trapped in the region of low turbulence close to a wall.

4.3.2. Large g_2^+—saltation region

The dimensionless group, g^+, can be viewed as representing the relative influences of gravity and turbulence in affecting the paths of particles injected into the fluid at the bottom boundary. For very large g^+ the influence of turbulence is small and the concentration field may be pictured

as resulting from a number of deterministic trajectories. This is the saltation regime which has received considerable attention in sediment transport.

The change of velocity along one of these trajectories is given as

$$\frac{dV_2}{dt} = -\frac{V_2}{\tau_p} - g. \tag{23}$$

Using the boundary condition that the initial value of V_2 at the wall is V_2^0, Eq. (23) can be solved to give

$$V_2 = (V_2^0 + g\tau_p)\exp\left(-\frac{t}{\tau_p}\right) - g\tau_p, \tag{24}$$

$$x_2 = \tau_p\left[(V_2^0 + g\tau_p)\left\{1 - \exp\left(-\frac{t}{\tau_p}\right)\right\} - gt\right]. \tag{25}$$

The time at which the particles deposit, t_d, is obtained by solving Eq. (25) for $x_2 = 0$. Since $R_{At} = 0$ in the saltation range, Eq. (14) can be written as

$$\frac{k_{DB}}{v^*} = \frac{R_{Ab}}{2C_B v^*}. \tag{26}$$

The concentration field at a given x_2 in the fully-developed region can be pictured as resulting from sources that entered the field at previous times of 0 to t_d. The bulk concentration is thus given as

$$C_B = \frac{R_{Ab}t_d}{2H} \tag{27}$$

and, after substituting Eq. (27) into Eq. (26)

$$k_{DB} = \frac{H}{t_d}, \tag{28}$$

where $R_{Ab}t_d$ is the number of particles admitted to the field per unit area over the time interval t_d. Since $V_2 = dx_2/dt$, the integration of Eq. (23) gives

$$V_2 = V_2^0 - \frac{x_2}{\tau_p} - gt. \tag{29}$$

When $x_2 = 0$ the particle strikes the wall. Thus, for the linear resistance law, used in Eq. (23), the velocity with which the particles hit the wall is given as

$$V_d = V_2^0 - gt_d. \tag{30}$$

This can be less than the free-fall velocity, $V_T = g\tau_p$.

5. Results

5.1. Calculation of concentrations

The computational experiment involved the injection of N_b (= 10000) particles from the bottom wall at time zero. Particles are treated as points that deposit when they are a distance of $d_p/2$ from a wall. When a part of these particles deposit at the top wall, an additional simulation of N_b (= 10000) particles injected from the top wall was performed. Fully-developed concentration fields are calculated by using the Lagrangian method described by Mito and Hanratty (2003). The relative strengths of the sources at the two walls are adjusted so as to satisfy Eq. (1) (Mito and Hanratty, 2003). Thus the rates of atomization at the bottom and top walls in the fully-developed field can be defined as $R_{Ab} = m_p N_b/A\Delta t$ and $R_{At} = m_p(R_{At}/R_{Ab})(N_b/A\Delta t)$, where A is the area of the wall over which the particles are discharged and Δt is the time interval over which N_b particles are admitted from the wall sources and m_p is the particle mass.

The concentration fields were calculated by using first-order weights, for each particle, that are defined by using the distances between the center of the particle and the sampling points between which the center of the particle exists. Fig. 7a shows sampling points y_{n-1}, y_n, y_{n+1}. When the center of the particle, y, exists between y_n and y_{n+1} in Fig. 7a, the weights $(y_{n+1} - y)/(y_{n+1} - y_n)$ and $(y - y_n)/(y_{n+1} - y_n)$ are, respectively, considered to contribute to the concentrations at y_n and y_{n+1}. This method improves the accuracy of sampling over what is realized with a zeroth-order method that considers a single weight (= 1) for each particle in a bin that ranges from y_n to y_{n+1}. It is noted that the first-order sampling is performed at points rather than bins and that the bin size characterizing the concentration at y_n can be specified as $\Delta y_n = (y_{n+1} - y_{n-1})/2$. For a point at the end of the whole sampling region, y_1, shown in Fig. 7b, the bin size can be specified as $\Delta y_1 = (y_2 - y_1)/2$. For calculations of concentration profiles the 129 sampling points are distributed from $x_2 = d_p/2$ to $x_2 = 2H - d_p/2$ with a cosine function, which gives bin sizes of $\Delta x_2^+ = 0.088$ at the walls and $\Delta x_2^+ = 14.4$ at the center of the channel. For calculations of the concentration at the wall, $\overline{C}_W$, defined at $x_2^+ = d_p^+/2 = 0.184$, an additional point is located at $x_2^+ = d_p^+/2 + 2 \times 10^{-4}$. With this definition $\overline{C}_W$ is calculated using particles between $x_2^+ = 0.184$ and $x_2^+ = 0.184 + 2 \times 10^{-4}$.

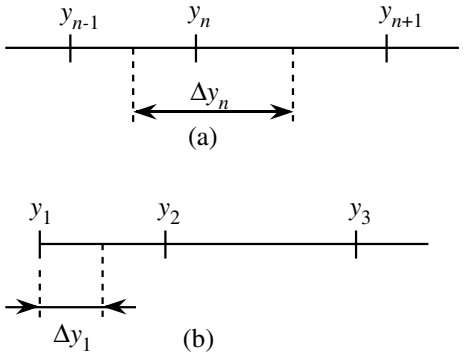

Fig. 7. Definition of bin sizes in the first-order sampling method: (a) for a point which does not exist at the end of the whole sampling region and (b) for a point at the end of the whole sampling region.

5.2. Results for zero gravity

Fig. 8 presents calculations for $g_2 = 0$ of the deposition constant, $k_{DB}^+ = k_{DB}/v^*$. In the range of $\tau_p^+ = 3$–10, k_{DB}^+ is observed to be strongly affected by τ_p^+. It increases from 4.4×10^{-4} at $\tau_p^+ = 3$ to 2.7×10^{-2} at $\tau_p^+ = 10$. The deposition constant becomes less sensitive to increases in τ_p^+ at large τ_p^+. The line constructed with dots and dashes was obtained from Eq. (21) with $V_T = 0$. That is, $k_D = \sigma_p/(2\pi)^{1/2}$, where σ_p^2 is the mean-square of the wall-normal velocity fluctuations of the particles at $x_2^+ = 40$. It is noted that this provides a good approximation for k_{DB}/v^* at large τ_p^+. This agreement supports the notion that deposition at large τ_p^+ is controlled by free-flights from locations outside the viscous wall layer.

Another deposition constant plotted in Fig. 8, $k_{DW}^+ = k_{DW}/v^*$, can be defined by using the concentration at the wall:

$$\frac{k_{DW}}{v^*} = \frac{R_D}{\overline{C}_W v^*}, \tag{31}$$

where $\overline{C}_W$ is calculated by using the bin adjacent to $d_p^+/2$. This may be looked upon as defining the wall boundary condition, $\overline{C}_W$, if R_D is fixed. The deposition constant, k_{DW}, is smaller than k_{DB} since $\overline{C}_W$ is larger than C_B. As shown in Part 1, this wall constant can be defined in terms of the average velocities of the injected particles, V_2^{0+}, and the average velocity of the other particles in the bin adjacent to the wall, $\overline{V}_W^+$

$$k_{DW}^+ = \left(\frac{1}{V_2^{0+}} - \frac{1}{\overline{V}_W^+}\right)^{-1}. \tag{32}$$

Particles are defined as striking the wall when they are at $x_2^+ = d_p^+/2 = 0.184$. Distribution functions of the wall-normal velocity components of these depositing particles at the wall, V_d^+, are calculated by using the first-order sampling method and 129 bins distributed from $V_d^+ = -2$ to 2 with a hyperbolic tangent function which gives bin sizes of $\Delta V_d^+ = 3.3\times10^{-5}$ at $V_d^+ = 0$ and $\Delta V_d^+ = 7.7\times10^{-2}$ at $V_d^+ = \pm2$. A probability density function can be defined for the rate of deposition, $r_D(V_d) = m_p n(V_d)/\Delta V_d \Delta t A$, where $n(V_d)$ is the number of particles with velocities between V_d and $V_d + \Delta V_d$ that are depositing over a time interval Δt and over an area of the wall A.

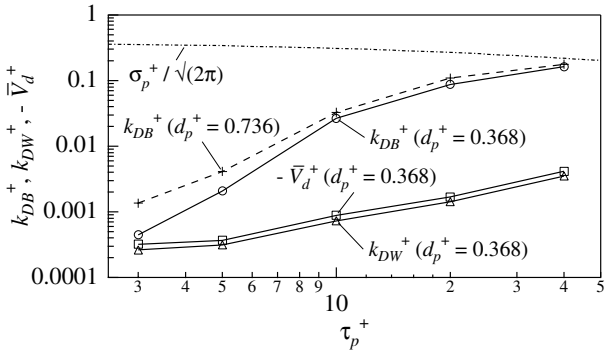

Fig. 8. Deposition constants, k_{DB}^+ and k_{DW}^+, and the average velocity of the deposition particles, $-\overline{V}_d^+$ for $V_T^+ = 0$.

This represents the contributions of the particles with different wall-normal velocities to the deposition flux since

$$R_{\mathrm{D}} = \int_{-\infty}^{0} \frac{m_{\mathrm{p}} n(V_{\mathrm{d}})}{\Delta V_{\mathrm{d}} \Delta t A} \mathrm{d}V_{\mathrm{d}} = \int_{-\infty}^{0} \mathrm{d}V_{\mathrm{d}} r_{\mathrm{D}}(V_{\mathrm{d}}). \tag{33}$$

Here the integral is defined for the negative semiinfinite range of velocities because all depositing particles have negative wall-normal velocity components.

Concentrations are defined for particles in finite or infinitesimal bins. When an average is taken for an ensemble of particles that pass a plane, such as defined by the distribution function $m_{\mathrm{p}} n(V_{\mathrm{d}})/\Delta V_{\mathrm{d}} \Delta t A$, the results are biased to favor higher velocity particles in the bin next to the plane. By noticing that the flux equals the product of the concentration and the velocity, a probability function representing the fraction of the depositing particles in the bin next to the wall which have velocities between V_{d} and $V_{\mathrm{d}} + \Delta V_{\mathrm{d}}$ can be defined as

$$\overline{C}_{\mathrm{d}} = -\int_{-\infty}^{0} \frac{\mathrm{d}V_{\mathrm{d}}}{V_{\mathrm{d}}} r_{\mathrm{D}}(V_{\mathrm{d}}) = -\int_{-\infty}^{0} P(V_{\mathrm{d}}) \mathrm{d}V_{\mathrm{d}}. \tag{34}$$

Thus $r_{\mathrm{D}}(V_{\mathrm{d}}) = m_{\mathrm{p}} n(V_{\mathrm{d}})/\Delta V_{\mathrm{d}} \Delta t A$ represents the pdf for the deposition flux and $P(V_{\mathrm{d}}) = r_{\mathrm{D}}(V_{\mathrm{d}})/V_{\mathrm{d}}$ represents the pdf for the concentration of depositing particles. From Eq. (34) the fraction of the depositing particles in the bin adjacent to wall that have velocities larger than V_{d} is given by

$$F_n(V_{\mathrm{d}}) = -\int_{V_{\mathrm{d}}}^{0} \frac{\mathrm{d}V_{\mathrm{d}}}{\overline{C}_{\mathrm{d}} V_{\mathrm{d}}} r_{\mathrm{D}}(V_{\mathrm{d}}). \tag{35}$$

From Eq. (35) the average V_{d} of the depositing particles in the bin next to the wall is given as

$$\overline{V}_{\mathrm{d}} = -\int_{-\infty}^{0} V_{\mathrm{d}} \frac{\mathrm{d}V_{\mathrm{d}}}{\overline{C}_{\mathrm{d}} V_{\mathrm{d}}} r_{\mathrm{D}}(V_{\mathrm{d}}) = -\frac{R_{\mathrm{D}}}{\overline{C}_{\mathrm{d}}}. \tag{36}$$

Similarly, from Eq. (33), the fraction of the flux contributed by particles with velocities larger than V_{d} is given by

$$F_r(V_{\mathrm{d}}) = -\int_{V_{\mathrm{d}}}^{0} \frac{\mathrm{d}V_{\mathrm{d}}}{R_{\mathrm{D}}} r_{\mathrm{D}}(V_{\mathrm{d}}). \tag{37}$$

Probability density functions for the concentration of depositing particles in the bin next to the wall, $P(V_{\mathrm{d}})$, are plotted in Fig. 9. The solid line represents the average of the negative components of the wall normal component of the fluid velocity fluctuations at $x_2^+ = d_{\mathrm{p}}^+/2$, that was calculated from a DNS at $Re_\tau = 150$ as 1.7×10^{-4}. All of the distributions have large peaks near this very small velocity. We, therefore, interpret these peaks as representing particles that are depositing by turbulent impaction, as described above and in Section 4.2.3. Cumulative fractions of the particles in the wall bin that are striking the wall, defined with Eq. (35), are plotted in Fig. 10a. From Fig. 9 we define particles with $-V_{\mathrm{d}}^+ \leqslant 1 \times 10^{-3}$ as depositing by turbulent impaction and particles with $-V_{\mathrm{d}}^+ > 1 \times 10^{-3}$ as depositing by free-flight. Fig. 10a, therefore, indicates that the 100.0%, 99.7%, 98.4%, 97.1% and 94.1% of the depositing particles will strike the wall by turbulent impaction for $\tau_{\mathrm{p}}^+ = 3$, 5, 10, 20, 40, respectively.

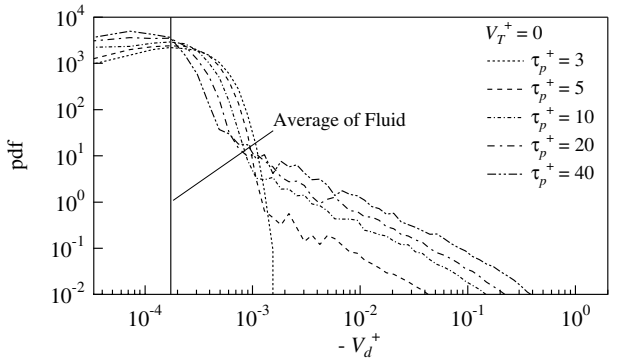

Fig. 9. Probability density functions of the depositing particles for $V_T^+ = 0$, where pdf $= -m_p n(V_d)/\overline{C}_d \Delta V_d \Delta t A V_d = P(V_d)/\overline{C}_d$.

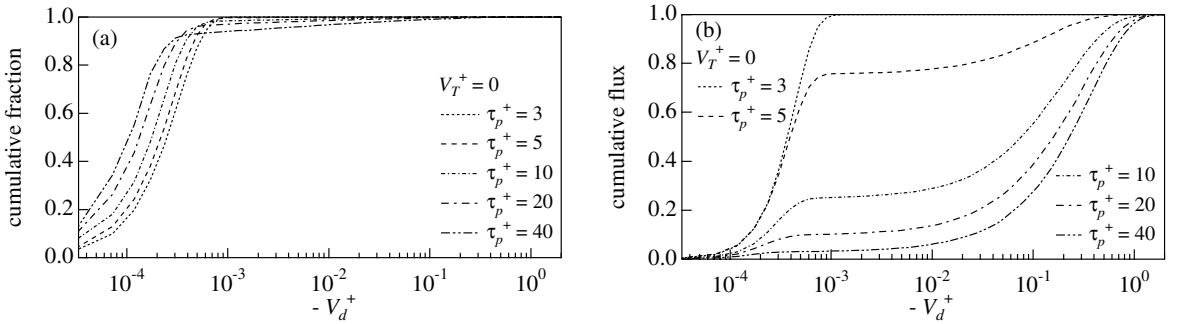

Fig. 10. Cumulative fractions (a) of the concentration of depositing particles with velocities $\geqslant V_d^+$, Eq. (35) and (b) of the contribution to the wall flux by particles with velocities $\geqslant V_d^+$, Eq. (37).

Of more interest are cumulative contributions to the deposition flux, R_D, defined by Eq. (37). These are shown in Fig. 10b. The ordinate represents the cumulative flux, normalized by R_D. For large $-V_d^+$ the curves in Fig. 10b converge to unity. The contributions to the fluxes by particles with velocities of $-V_d^+ \leqslant 1 \times 10^{-3}$ are 99.8%, 75.8%, 25.2%, 10.2%, 3.3% for $\tau_p^+ = 3$, 5, 10, 20, 40, respectively. From these results we conclude that, for the situations considered in this paper, turbulent impaction is the dominant mechanism of deposition for $\tau_p^+ \leqslant 5$. It is noted that the free-flight mechanism is very important for $\tau_p^+ \geqslant 10$, even though the concentration of free-flight particles at the wall is very small.

Average velocities of depositing particles, defined by Eq. (36), are plotted in Fig. 8. If the bin close to the wall is small enough all of the particles that are not being injected are moving toward the wall so $\overline{V}_d^+ \cong \overline{V}_W^+$. From Eq. (32) it is seen that $k_{DW}^+ = -\overline{V}_W^+$ since the injected particles are making a negligible contribution to the concentration at the wall. The slight difference between k_{DW}^+ and $-\overline{V}_d^+$ suggests that the sampling bin at the wall contains particles which are stagnant or have extremely small positive velocities.

5.3. Effect of gravity

5.3.1. R_{At}/R_{Ab} (or R_{Dt}/R_{Db})

Fig. 11 presents ratios of the rates of atomization at the top wall, R_{At} $(= R_{Dt})$, to those at the bottom wall, R_{Ab} $(= R_{Db})$, as functions of g^+. For $Re_\tau = 590$ and $\tau_p^+ \geqslant 5$, the largest value of g^+ for which particles strike the top wall is approximately equal to 0.012.

The inequality of R_{Db} and R_{Dt} can be associated with two factors: (1) gravity enhances deposition at the bottom wall and inhibits deposition at the top wall, (2) gravity causes the concentration profile of drops to be asymmetric. Pan and Hanratty (2002) have observed that asymmetry of the concentration profiles increases with increasing V_T^+. Our calculations confirm this and show that asymmetry is first observed for $V_T^+ \cong 0.01$, which is indicated by the vertical lines in Fig. 11. It is noted that large decreases in R_{At}/R_{Ab} can be observed for increasing g^+ in regions where the concentration profiles are symmetrical. However the decreases become more pronounced after the profiles lose their symmetry. Thus, the sharp decreases in the ratio at $g^+ \cong 2.5 \times 10^{-4}$ and $g^+ \cong 5 \times 10^{-4}$ for $\tau_p^+ = 40$, 20 are associated with the onset of asymmetry effects.

The limiting g^+ observed for $\tau_p^+ = 3$ particles to strike the top wall is very different from what is observed for the larger τ_p^+ particles represented in Fig. 11. This is because deposition is controlled by turbulent impaction rather than free-flight. Particles reach the vicinity of the top wall at much larger g^+ than the limiting value. For example, at $g^+ = 0.014$ particles are found at a distance of $x_2^+ = 1.8$ from the top wall and tend to accumulate just beyond this location. Deposition occurs at the top wall when turbulent velocities are larger than gravitational settling, equal to $g^+\tau_p^+$. In Section 5.1 we estimated that turbulent impaction velocities should be of the order of 1.7×10^{-4}. This provides an estimate of $g^+ = 5.7 \times 10^{-5}$ as a limiting value for $\tau_p^+ = 3$ particles to strike the top wall, consistent with results given in Fig. 11.

The above reasoning suggests that when free-flight is no longer an effective mechanism V_T^+ (rather than g^+) approximately defines the condition for which particles will no longer impact on the top wall. The result for $\tau_p^+ = 3$ gives a critical V_T^+ of the order of 1.7×10^{-4}.

5.3.2. Rates of deposition

Deposition constants defined with bulk concentrations, k_{DB}^+ $(= k_{DB}/v^*)$, plotted against g^+ in Fig. 12a and against V_T^+ in Fig. 12b, show the influence of gravity on rates of deposition. It is convenient to consider three regimes: (1) for $V_T^+ <$ ca. 0.01 the particles may be considered to be symmetrically distributed, even though R_{At}/R_{Ab} may not equal unity. (2) For $g^+ >$ ca. 4×10^{-2} a saltation region exists. (3) An intermediate region, which includes situations for which particles do not reach the top wall, can be defined for $V_T^+ >$ ca.0.01 and $g^+ <$ ca. 4×10^{-2}. Regimes 1 and 2 are identified in Fig. 12a and b by solid lines. The dashed line indicates the condition required for particles characterized by $\tau_p^+ \geqslant 5$ to reach the top wall. We designate this as a transition to annular flow.

Fig. 13 compares calculations with theoretical predictions for the saltation region. These calculations differ from those presented in Section 4.3.2 in that Stokes law is not used to calculate the drag on the particles. Excellent agreement between theory and the stochastic calculations is noted if $g^+ \geqslant$ ca. 0.04. The particle trajectories do not intercept the top wall in the saltation region and the peaks of the trajectories move closer to the bottom wall as g^+ increases.

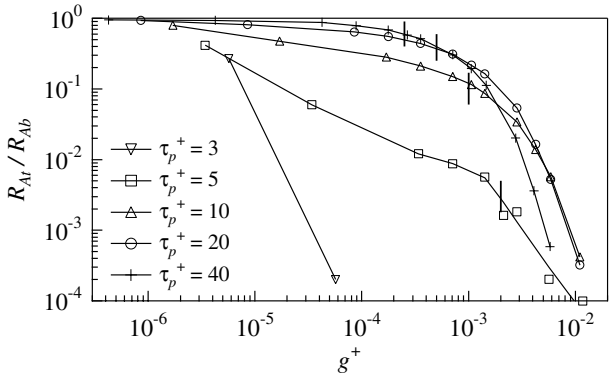

Fig. 11. Ratios of the rates of atomization at the top and bottom walls.

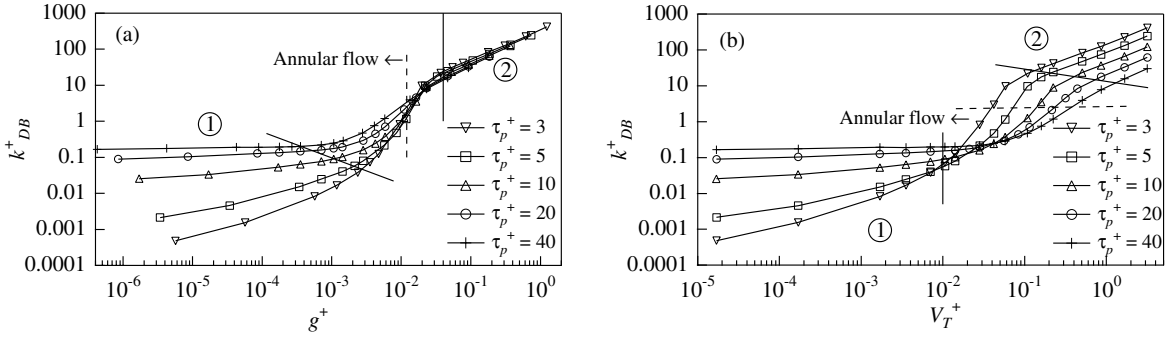

Fig. 12. Deposition constants defined with the bulk concentrations: (a) effect of g^+ and (b) effect of V_T^+.

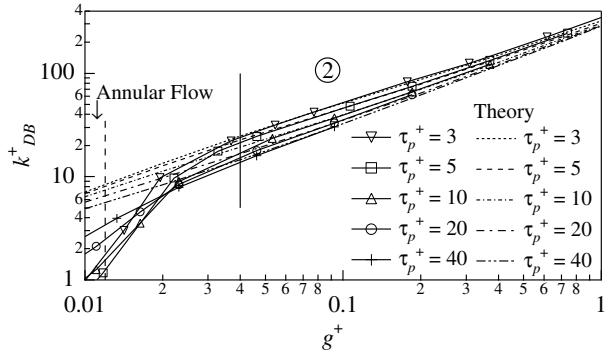

Fig. 13. Deposition constants defined with the bulk concentrations in the saltation regime.

The striking feature of Fig. 12 is the strong effect that gravity can have on the deposition constant even for small V_T^+ for which the concentration profile is approximately symmetric (Regime 1). Thus for $\tau_p^+ = 3$, 5, 10 the deposition constants at $V_T^+ = 0.01$ are, respectively, 162, 28

and 3.4 times the values observed for $V_T^+ = 0$. The reason for this is the enhancement of the deposition velocity at the bottom wall. The largest changes in k_{DB}^+ are seen in Regime 3 where enhancements in the deposition rate at the bottom wall, with increasing g^+, are associated both with increasing deposition velocities and with increasing asymmetry of the concentration profile. The latter effect redistributes the particles so that there are larger concentrations in the bottom regions of the channel where deposition is larger.

5.3.3. Velocities of depositing particles

Insights about how gravity affects deposition rates can be obtained by examining the velocity of depositing particles on the bottom wall. Fig. 14a shows how the average velocity with which particles strike the bottom wall, $\overline{V}_d^+$, depends on V_T^+ and τ_p^+. The straight line indicates the condition $-\overline{V}_d^+ = V_T^+$. For $\tau_p^+ = 3$, 5 the velocity $\overline{V}_d^+$ at very small V_T^+ is representative of the turbulent velocity fluctuations very close to the wall. (See Section 5.1.) Gravitational settling provides another means to deposit particles. It can dominate at large V_T^+ where $\overline{V}_d^+ = -V_T^+$. The average velocities for $\tau_p^+ = 3$ and for $\tau_p^+ = 5$ almost agree because the effect of free-flight on deposition, which could be a function of τ_p^+, is very small for these τ_p^+.

For larger τ_p^+, free-flight controls deposition for very small V_T^+. Gravitational settling provides a means of depositing particles that are trapped in the viscous sublayer, so the number of particles that deposit is increased. If the settling velocities are less than the free-flight velocities the average velocities of the depositing particles slightly decrease with increasing V_T^+. However, at large V_T^+ gravitational settling dominates. For $\tau_p^+ \geqslant 10$ the average velocity of the depositing particles increases with increasing τ_p^+ because the contribution of the free-flight particles to deposition increases. At very large g^+, the saltation region exists for which the particles are not in the field long enough to reach free-fall, so $-\overline{V}_d^+ < V_T^+$. This is illustrated in Fig. 14b where the calculations are compared with the saltation theory. Excellent agreement is noted at large V_T^+.

Probability density functions characterizing $-V_d^+$, presented in Fig. 15, provide a more detailed understanding of how gravity enhances deposition. The distribution functions in Fig. 15a are for a free-fall velocity which is of the same order as the velocities characterizing turbulent impaction, $V_T^+ = 1.7 \times 10^{-4}$. Qualitatively the distribution functions are the same as observed for $V_T^+ = 0$ in Fig. 9. Fig. 15b presents results for $V_T^+ = 0.014$, which is much larger than the velocities characterizing turbulent impaction. From Fig. 14a it is seen that $-\overline{V}_d^+ = V_T^+$ for $\tau_p^+ = 3$, 5 when

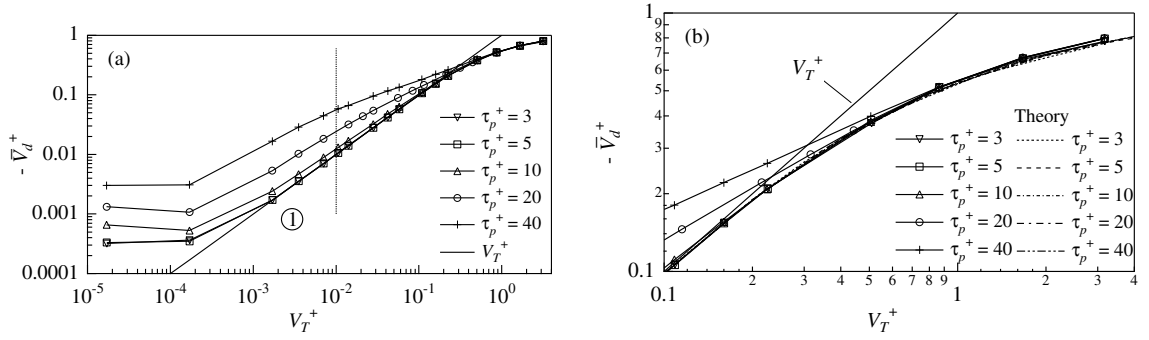

Fig. 14. Average velocities of the particles depositing on the bottom: (a) all regimes and (b) saltation regime.

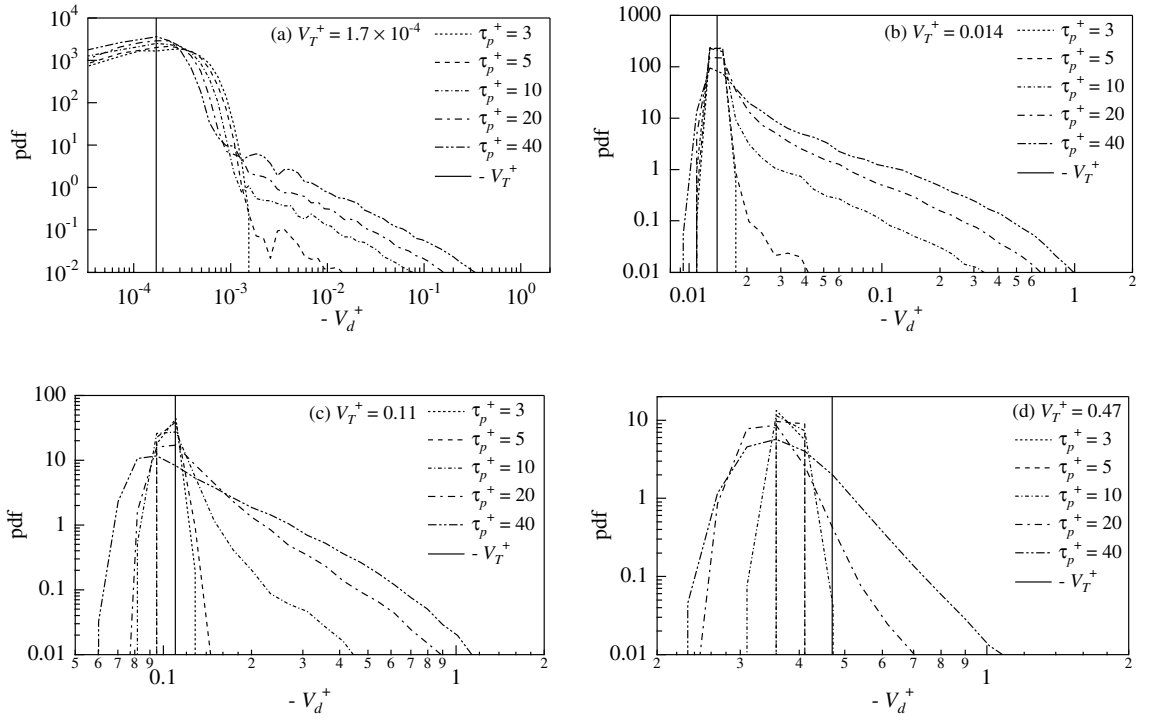

Fig. 15. (a)–(d): probability density functions for the velocities of particles depositing on the bottom wall, where $\text{pdf} = -m_p n(V_d)/\overline{C}_d \Delta V_d \Delta t A V_d = P(V_d)/\overline{C}_d$. (a) $V_T^+ = 1.7 \times 10^{-4}$, (b) $V_T^+ = 0.014$, (c) $V_T^+ = 0.11$, (d) $V_T^+ = 0.47$.

$V_T^+ = 0.014$. The striking feature in Fig. 15b is that turbulent impaction does not occur. All of the particles that are trapped near the wall are carried to the wall by gravitational settling and there is a peak at V_T^+ for all τ_p^+. For $\tau_p^+ = 3$, 5 the contributions by free-flight are negligibly small so that gravitational settling is the only mechanism for deposition. Fig. 15c, for $V_T^+ = 0.11$, represents a situation where $-\overline{V}_d^+ = V_T^+$ for $\tau_p^+ = 3$, 5, 10. There is a peak at V_T^+ for all of the calculations except for $\tau_p^+ = 40$. Significant contributions are made by free-flight for $\tau_p^+ = 20$, 40 so that $-\overline{V}_d^+ > V_T^+$. The results for $V_T^+ = 0.45$, in Fig. 15d, are for a situation which is in the saltation regime or close to it. It is noted that the distribution function tends to peak at values of $-V_d^+$ which are less than V_T^+ and that free-flight contributions are still important for $\tau_p^+ = 40$.

5.3.4. Deposition constants for the top wall

The rate constant k_{DB}^+ represents an average of the rates of deposition at the bottom and top walls. In order to consider the rates separately, we chose a distance of $x_2^+ = 40$ to define a representative concentration outside the viscous sublayer. Rate constants for the bottom and top walls,

$$\frac{k_{Db40}}{v^*} = \frac{R_{Ab}}{C_{b40} v^*}, \tag{38}$$

$$\frac{k_{Dt40}}{v^*} = \frac{R_{At}}{C_{t40} v^*}, \tag{39}$$

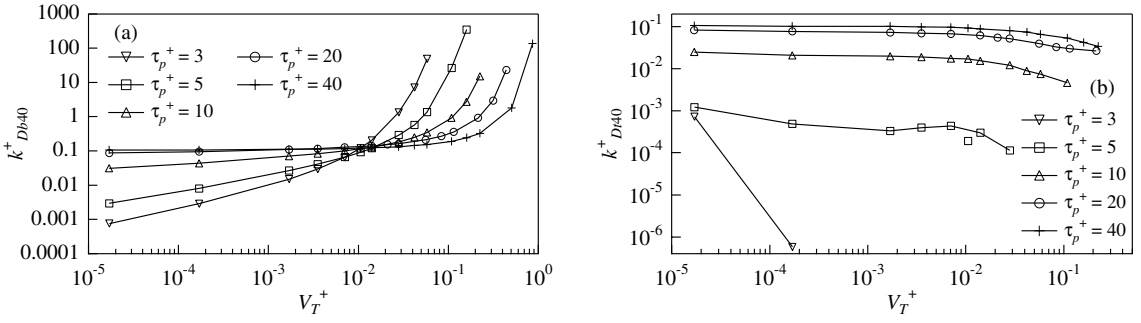

Fig. 16. Deposition constants defined with the concentrations at a distance of $x_2 = 40$ from the bottom and top walls, k^+_{Db40} and k^+_{Dt40}.

are plotted against V_{T}^+ in Fig. 16. These constants cannot be calculated at large V_{T}^+, for which $C_{\mathrm{b40}} = 0$, $C_{\mathrm{t40}} = 0$. The shapes of the profiles of k^+_{Db40} are similar to those for k^+_{DB} (Fig. 12b) except for the absence of results at large V_{T}^+. An interesting aspect of Fig. 16 is that the deposition constant for the top wall does not show large variations with V_{T}^+ for $\tau_{\mathrm{p}}^+ \geqslant 5$. However, as seen in Fig. 11, the rates of deposition at the top wall decrease strongly with increasing V_{T}^+. Thus for $V_{\mathrm{T}}^+ = 0.11$ and $\tau_{\mathrm{p}}^+ = 40$ the ratio $R_{\mathrm{At}}/R_{\mathrm{Ab}} = 0.020$. For $V_{\mathrm{T}}^+ = 0.51$ and $\tau_{\mathrm{p}}^+ = 40$ no particles strike the top wall.

These results can be understood by considering the mechanisms for particle deposition already discussed. When $g^+ = 0$, particles are deposited at the bottom wall by turbulent impaction and free-flight. When $g^+ \neq 0$, gravitational settling deposits particles entrapped close to the bottom boundary. Thus for relatively small g^+ gravity and free-flight are controlling. At the top boundary gravity opposes deposition. Thus particles that accumulate close to the top wall are prevented from reaching the wall and deposition occurs by free-flight. For $g^+ = 0$, $\tau_{\mathrm{p}}^+ = 3$ deposition occurs only by turbulent impaction and the deposition constant, k^+_{Dt40}, is seen to fall to zero at a very small V_{T}^+. Free-flight is observed to be the important mechanism for deposition at the top wall for $\tau_{\mathrm{p}}^+ \geqslant 5$, even though its effect on deposition at the bottom wall is very small for $\tau_{\mathrm{p}}^+ = 5$. For $\tau_{\mathrm{p}}^+ \geqslant 5$ the rate of deposition increases with increasing τ_{p}^+.

6. Concluding remarks

Calculations for $g_2 = 0$ produce similar results to what is observed for a vertical flow. Deposition constants are found to increase dramatically with τ_{p}^+. It was found that for $\tau_{\mathrm{p}}^+ = 3$–40 the particles accumulate in a layer close to the wall where they have a jittering motion due to local turbulence. They, therefore, strike the wall with velocities of the order of the fluid velocity fluctuations at $d_{\mathrm{p}}^+/2$.

Particles that arrive at the wall by free-flight have much larger velocities so they can make much larger contributions to the wall flux than would be anticipated from their small concentration. Thus, for $\tau_{\mathrm{p}}^+ = 20$, 40 free-flight provides 89.8% and 96.7% to the flux of depositing particles. At large τ_{p}^+ free-flights begin at locations outside the viscous wall layer with velocities characteristic of the turbulence in the outer flow. For $\tau_{\mathrm{p}}^+ = 3$ free-flight particles contribute only 0.2% of the flux

so the rate of deposition is controlled by turbulent impaction. Intermediate behavior is observed for $\tau_p^+ = 10$, 5 for which free-flight contributes 74.8%, 24.2% of the flux.

Gravity affects deposition rates because it changes deposition velocities and causes an asymmetric distribution of particles. The most striking example of this is the large increase of deposition constants with increasing V_T^+ at very small V_T^+ where the concentration profile is symmetric. This occurs because gravity provides an efficient mechanism to deposit particles that, otherwise, would be trapped in a layer close to the wall.

When V_T^+ is large enough to cause asymmetries a further enhancement of deposition rates is noted. At $g^+ > 0.012$ the particles cannot reach the top wall. This could provide a necessary condition for the development of an annular flow. For $g^+ > 0.04$ a saltation region exists which is described quite well by theory.

Dimensionless concentrations can be defined as $\overline{C}v^*/R_{Ab}$. A knowledge of the spatial variation of these dimensionless concentrations with distance from the bottom wall can be used to calculate deposition constants.

Results of exploratory studies which look at the effects of d_p^+, V_i^{0+} and Re_τ are given in Appendices A and B, with an emphasis on identifying mechanisms controlling deposition and dispersion.

Acknowledgements

This work is supported by the DOE under grant DEFG02-86ER 13556. Computer resources have been provided by the National Center for Supercomputing Applications located at the University of Illinois.

Appendix A. Effects of changes in d_p^+

Increases in d_p^+ affect the concentration field and the rate of deposition because the time constant, τ_p^+, and the distance of the particle center from the wall at deposition increase. Calculations were done for $d_p^+ = 0.368$ and 0.736 to examine this influence.

These showed no changes in the deposition constant unless $V_T^+ \leqslant 2 \times 10^{-5}$. The chief effect is that deposition by turbulent impaction is enhanced because the particle sees larger fluid turbulence when it is hitting the wall. At $V_T^+ = 0$, where the influence is a maximum, deposition constants for $\tau_p^+ = 3$, 5, 10, 20 and 40 are, respectively, increased by 204%, 98%, 23%, 25% and 9% when d_p^+ is increased from 0.368 to 0.736. (See Fig. 8.) The slight increase of the percentage from $\tau_p^+ = 10$ to 20 is caused by the increase of the contribution from free-flight particles. It is observed that the number of the particles that deposit by free-flight with large velocities increases with increasing d_p^+ for $\tau_p^+ = 10$, 20, 40.

Appendix B. Effects of changes in V_i^{0+} and Re_τ

The deposition constant was found to be insensitive to changes in the streamwise component of the injection velocity, V_1^{0+}. (Results did not change for $V_1^{0+} = 0$, 7.5 and 15 for $\tau_p^+ = 20$.) Results on

the effect of V_2^{0+} are shown in Fig. 17. Increases in V_2^{0+} have the effect of injecting the particles to a larger distance from the wall before they start to mix due to turbulence. Decreases in g^+ (or of V_T^+) indicate an increase in the effects of turbulence relative to the effects of gravity. Both of these cause increases in the concentration of the particles and, therefore, decreases in k_{DB}^+. It is noted in Fig. 17 that changes in V_2^{0+} have a small effect for small V_T^+ and very large effect in the saltation region.

Calculations were carried out for $Re_\tau = 150$, $V_T^+ = 0$–3.2 and $\tau_p^+ = 20$. These yield much smaller k_{DB}^+ than shown in Fig. 12 for $Re_\tau = 590$, $V_T^+ = 0$–3.2 and $\tau_p^+ = 20$. The reason for this is that the concentration profiles are governed by two length scales, ν/v^* and H. Fig. 18a plots the dimensionless concentration versus x_2^+. For $Re_\tau = 150$ the top of the channel is located at $x_2^+ = 300$. For $Re_\tau = 590$ it is at $x_2^+ = 1170$. The concentration fields for $Re_\tau = 150$ and 590 show similarity at $x_2^+ < 50$. Fig. 18b plots the dimensionless concentration against x_2/H. Because of the similarity for the wall profiles which are governed by the length scale ν/v, a larger concentration appears for $Re_\tau = 150$ in the near-wall region of this plot. A similarity between the concentration profiles is observed in the center region of the channel at which a constant turbulent diffusivity, $\varepsilon_t/v^*H = 0.085$ is controlling for both profiles. It is noted that the turbulent diffusivity in the center region is uniquely decided for the two Reynolds numbers by using the global scale, H. The profiles in the center region, which are described with exponential functions, are matched to the wall profiles through the buffer regions. From the definition given by Eq. (10) and Fig. 18a, it is noted that $C_B v^*/R_{Ab}$ would be larger (and k_{DB}^+, smaller) for $Re_\tau = 150$.

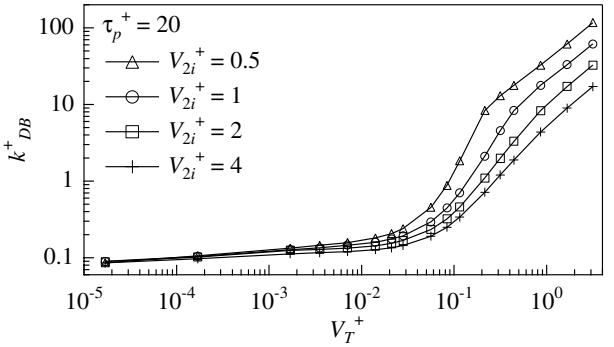

Fig. 17. Influences of the wall-normal component of the injection velocity on the rate of deposition for $\tau_p^+ = 20$.

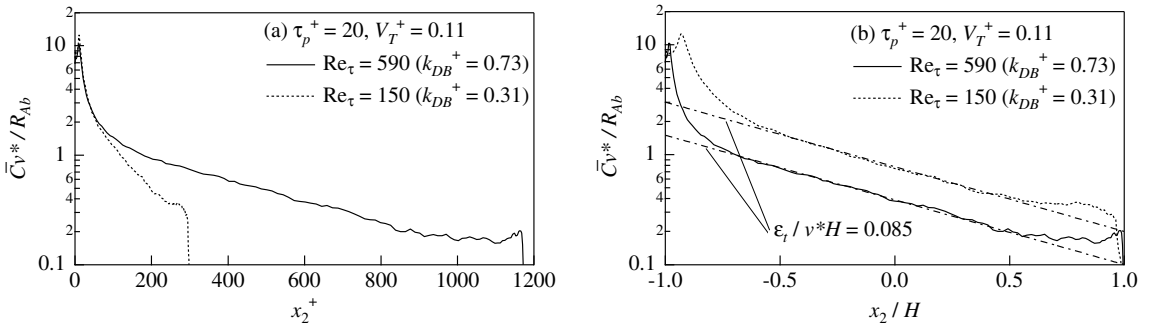

Fig. 18. Concentration profiles at $Re_\tau = 150$ and 590 for $\tau_p^+ = 20$, $V_T^+ = 0.11$.

References

Baik, S., Hanratty, T.J., 2003. Concentration profiles of droplets and prediction of the transition from stratified to annular flow in horizontal pipes. Int. J. Multiphase Flow 29, 329–338.

Brooke, J.W., Hanratty, T.J., McLaughlin, J.B., 1994. Free-flight mixing and deposition of aerosols. Phys. Fluids 6, 3404–3415.

Chen, M., McLaughlin, J.B., 1995. A new correlation for the aerosol deposition rate in vertical ducts. J. Colloid Interface Sci. 169, 437–455.

Hay, K.J., Liu, Z.C., Hanratty, T.J., 1996. Relation of deposition to drop size when the rate law is nonlinear. Int. J. Multiphase Flow 22, 829–848.

Iliopoulos, I., Mito, Y., Hanratty, T.J., 2003. A stochastic model for solid particle dispersion in a nonhomogeneous turbulent field. Int. J. Multiphase Flow 29, 375–394.

Lee, M.M., Hanratty, T.J., Adrian, R.J., 1989a. The interpretation of droplet deposition measurements with a diffusion model. Int. J. Multiphase Flow 15, 459–469.

Lee, M.M., Hanratty, T.J., Adrian, R.J., 1989b. An axial viewing photographic technique to study turbulence characteristics of particles. Int. J. Multiphase Flow 15, 787–802.

McCoy, D.D., Hanratty, T.J., 1977. Rate of deposition of droplets in annular two-phase flow. Int. J. Multiphase Flow 3, 319–331.

Mito, Y., Hanratty, T.J., 2002. Use of a modified Langevin equation to describe turbulent dispersion of fluid particles in a channel flow. Flow Turbul. Combust. 68, 1–26.

Mito, Y., Hanratty, T.J., 2003. A stochastic description of wall sources in a turbulent field: part 1 Verification. Int. J. Multiphase Flow 29, 1373–1394.

Monin, A.S., Yaglom, A.M., 1975. In: Statistical Fluid Mechanics, vol. 1. M.I.T. Press, Cambridge.

Moser, R.D., Kim, J., Mansour, N.N., 1999. Direct numerical simulation of turbulent channel flow up to $Re_\tau = 590$. Phys. Fluids 11, 943–945.

Narayanan, C., Lakehal, D., Botto, L., Soldati, A., 2003. Mechanisms of particle deposition in a fully developed turbulent open channel flow. Phys. Fluids 15, 763–775.

Pan, L., Hanratty, T.J., 2002. Correlation of entrainment for annular flow in horizontal pipes. Int. J. Multiphase Flow 28, 385–408.

Paras, S.V., Karaberas, A.J., 1991. Droplet entrainment and deposition in horizontal annular flow. Int. J. Multiphase Flow 17, 455–468.

Perkins, R.J., 1992. The entrainment of heavy particles into a plane turbulent jet. In: Sommerfeld, M. (Ed.), Proceedings of the 6th Workshop on Two-Phase Flow Predictions. Erlangen, pp. 18–33.

Pozorski, J., Minier, J.P., 1998. On the Lagrangian turbulent dispersion models based on the Langevin equation. Int. J. Multiphase Flow 24, 913–945.

Shaw, D.A., Hanratty, T.J., 1977. Turbulent mass transfer rates to a wall for large Schmidt numbers. AIChE J. 23, 28–37.

Sommerfeld, M., Kohnen, G., Rüger, M., 1993. Some open questions and inconsistencies of Lagrangian particle dispersion models. In: Proceedings of the Ninth Symposium on Turbulent Shear Flows. Kyoto Japan, Paper No. 15–1.

Tennekes, H., 1979. The exponential Lagrangian correlation function and turbulent diffusion in the inertial subrange. Atmos. Environ. 13, 1565–1567.

Wang, Q., Squires, K.D., Chen, M., McLaughlin, J.B., 1997. On the role of the lift force in turbulence simulations of particle deposition. Int. J. Multiphase Flow 23, 749–763.

Williams, L.R., Dykhno, L.A., Hanratty, T.J., 1996. Droplet flux distributions and entrainment in horizontal gas–liquid flows. Int. J. Multiphase Flow 22, 1–18.

Zhang, H., Ahmadi, G., 2000. Aerosol particle transport and deposition in vertical and horizontal turbulent duct flows. J. Fluid Mech. 406, 55–80.